# 4. Raman Spectroscopy

Raman spectroscopy is a widely used tool to characterize material composition, sample temperature, and strain from analysis of the material specific phonon mode energies[1]. It requires very little sample preparation and a rapid, non-destructive optical spectrum is easily achieved.

Raman scattering is a weak interaction, and typically less than one in a million of the incoming photons exchanges energy with the phonons in bulk materials. The incoming light interacts with an electron that makes a virtual or real transition to a higher energy, where the electron interacts with a phonon (via electron-phonon coupling) before making a transition back to the electronic ground state. In this instantaneous process, energy and momenta are conserved so that $E_{scattered}=E_{laser}\pm h\Omega$ for Stokes (-) and Anti-Stokes (+) scattering respectively, with $\Omega$ being the frequency of the particular phonon mode. The energy of the inelastically scattered light is measured with respect to the laser energy (in $cm^{-1}$), and by convention, the stronger signal from the loss side (Stokes) is counted as positive. The choice of laser energy (typically in the visible or near-infrared) does not affect the Raman shift, but if the laser energy is resonant with an electronic transition, the Raman intensity can be increased by many orders of magnitude. In a one-dimensional system such as carbon nanotubes where the density of states is strongly peaked, resonance Raman scattering dominates over non-resonant contributions. Hence, resonance Raman scattering from nanotubes gives information of the vibrational mode from the Raman shift, as well as of the optical transition energy since it is close to the energy of the laser.

This section is meant to give a brief background to resonant Raman scattering applied to carbon nanotubes and practical advice on how to do the measurements, while discussing some pitfalls to be aware of when interpreting data. While Raman scattering can be used for quantitative measurements, most standard measurements give relative and qualitative information that is best used for comparisons of similar samples in the same sample state (e.g. in ropes, powders, solution, polymers etc.)

The most prominent Raman active peaks in carbon nanotubes are the low frequency, radial breathing modes (RBM) and the higher frequency, D, G and G' modes. While D, G, and G' modes are also found in graphite, the RBM mode is a unique carbon nanotube mode. A study of the RBMs gives information regarding the distribution of nanotube diameters in a given sample. Due to the resonance behavior of the Raman intensity, several laser lines need to be used to determine the extent of the diameter distribution. The relative strength and width of the D band mode also gives a qualitative measurement of how large fraction of graphitic material and nanotubes with defects are present in the sample. Fig 1 shows Raman spectra from HiPCo powder where the RBM, D, G and G' bands are shown.

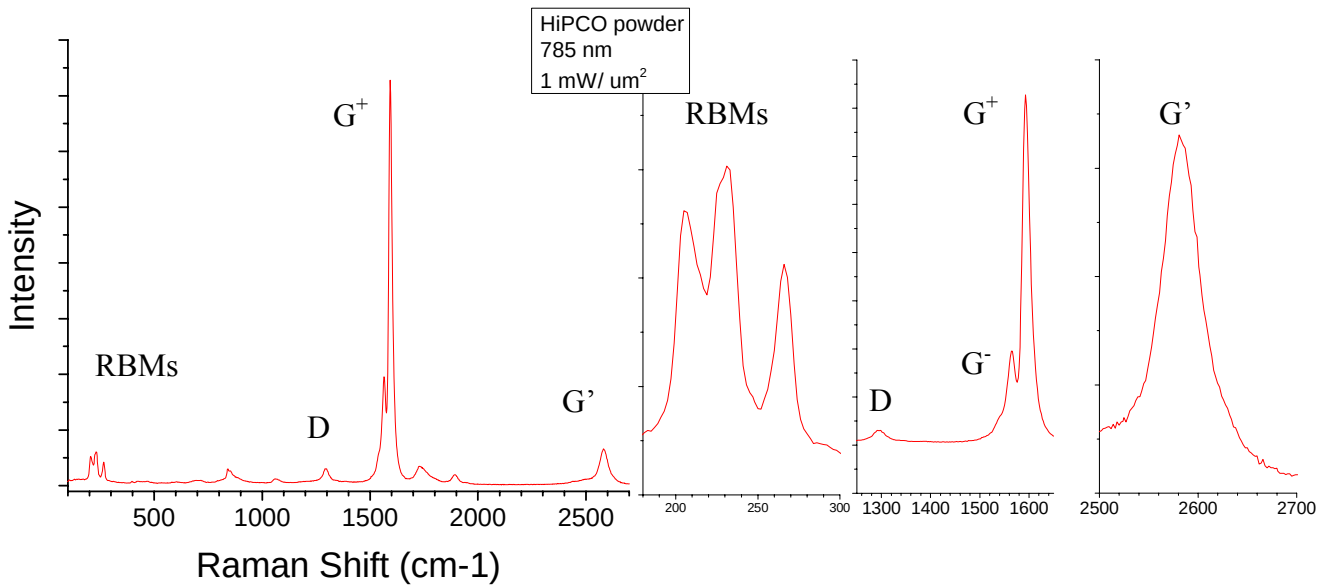


**Figure. 1.** Raman spectra of carbon nanotubes.

## 4.1 Resonant Raman Scattering in Carbon Nanotubes

**Electronic structure**
One of the more intriguing aspects of carbon nanotubes is they can be either metallic or semiconducting with variable and direct bandgap. Depending on the chirality (n,m) the nanotubes are metallic when n-m= 3k (k=integer) and semiconducting otherwise. This essential feature of the electronic structure is readily obtained from considering the electronic structure of graphite and then applying chirality dependent quantization of the allowed electron states in the confined directions. The one-dimensional electron bands lead to sharp peaks in the joint electronic density of states, the so-called van Hove singularities, which are labeled $E_{ii}$ with i=1,2,3,… numbering the valence and conduction sub-bands[2]. The singularities provide for strong resonant enhancement of the otherwise weak Raman signal. The $E_{ii}$ is roughly proportional to 1/diameter, and are often plotted against the nanotube diameter, in what is called a Kataura plot.

**Exciton versus band edge resonance** It has recently been demonstrated experimentally that optical transitions in nanotubes between the van Hove singularities are modified by electron-hole interaction with very large binding energies[3]. As is typical for a 1D system, the entire optical oscillator strength gets transferred from the band edge absorption $E_{ii}$ to the exciton absorption energy, $E_{ii}$- $E_{binding}$. While this has far-reaching consequences for e.g. optically generated transport measurements, it does not significantly affect the analysis of

resonant Raman scattering [4]. The main difference is that the resonance occurs with the associated lowest bright exciton rather than the band edge energy $E_{ii}$. For simplicity, we will continue to refer to the optical transition energies as $E_{ii}$ rather than excitons. However, it is important to keep in mind that the excitonic resonance energies are dependent on the tube's local environment. For example, screening effects change the energies for tubes in different environments, e.g. dry powder versus individual tubes in solution or in air. Other environmental changes such as heating or cooling, strain, etc., also tend to shift the resonance energies. The implication is that a tube can move in and out of resonance by changing the environmental surroundings of the tube. For example, Raman signal from the (10,2) specie is observed with a 785 nm laser line for a nanotube bundle, but the signal disappears when the tubes are dispersed in solution. Hence, the Raman signal will originate from a different subset of an ensemble when the environment changes sufficiently. Examples of how the resonance energy changes for individual tubes in solution and in bundles are shown in the appendix.

**Resonance Raman profile**. Scanning the laser energy through an optical resonance gives the resonance excitation Raman profile for a given carbon nanotube phonon mode. Unlike photoluminescence excitation profiles where the center of the profile coincide with the optical transition $E_{ii}$, the Raman excitation profiles have two contributions; electronic resonance with the incoming laser light, ( $E_{laser} = E_{ii}$) and electronic resonance with the scattered light, which is shifted by a phonon-energy: $E_{scattered} = E_{laser} \pm h\Omega = E_{ii}$ . Hence, the center of the resonance profile is $E_{ii} \pm h\Omega/2$.

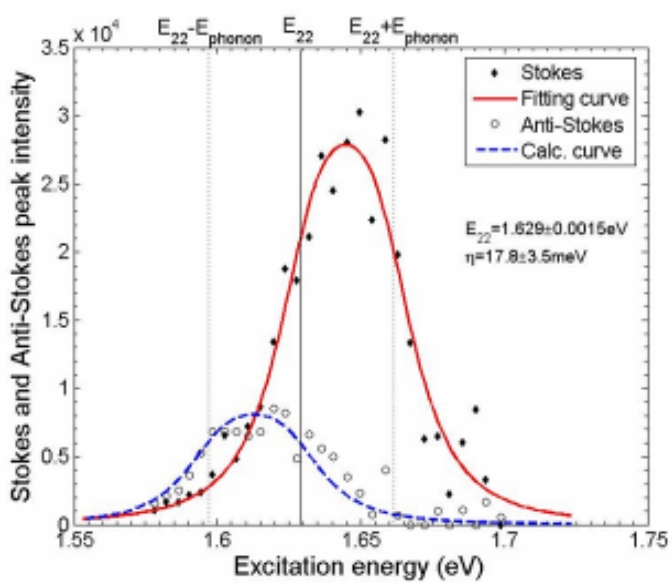


Fig 2. Resonance excitation profile. The curves show the Stokes (red) and Anti-Stokes (blue) resonance excitation profiles for (9,4) nanotube with RBM = 257 $cm^{-1}$.[5]

## 4.2 Raman-Active Modes in Carbon Nanotubes (RBM, D, G and G')

Carbon nanotubes have a rich Raman spectrum, but here we will only discuss the most well-known bands. For an extensive review of the Raman scattering from nanotubes, see [6]. The parent material to carbon nanotubes is graphite, which has several phonon modes that are Raman active. The most prominent modes are the G-band (G-graphite), the D-band (D-disorder) and the G' band (second-order Raman scattering from D-band vibrations). In addition to the graphite modes, carbon nanotubes have a unique, prominent, phonon mode due to isotropic radial expansion of the tube, which is called the radial breathing mode (RBM). The RBM frequency is inversely proportional to the diameter of the tube, making it an important feature for determining the diameter distribution of a sample. Its absence in other graphitic forms makes it a useful diagnostic for confirming the presence of nanotubes in a sample. Below, each Raman-active mode will be discussed further.

### 4.2.1 Radial breathing mode (RBM)

The RBM mode is the real signature of the presence of carbon nanotubes in a sample, since it is not present in graphite. The group theoretical notation is $A_{1g}$ and it is often called the "breathing" mode. The RBM frequency ($\omega$) is inversely proportional to the nanotube diameter with the relation

$$\omega(\mathrm{cm}^{-1}) = A/\mathrm{dia}(\mathrm{nm}) + B(\mathrm{cm}^{-1})$$

where the constants *A* and *B* have been determined experimentally with A= 223 $\mathrm{cm}^{-1}$/nm, B=10 $\mathrm{cm}^{-1}$. Several groups have found slightly different best fits of A and B, but for tube diameters between 0.8-1.3 nm, they give nearly identical frequency-diameter results. Most experimental systems that use a single grating spectrometer with a holographic notch filter for laser line rejection are limited to Raman frequencies larger than 100 -120 $\mathrm{cm}^{-1}$, which restricts the range of diameters that can be measured to smaller than ~ 2 - 2.5 nm. The use of multi-grating systems can lower the possible observed frequencies, thereby permitting larger tubes to be studied.

Several groups have mapped the transition energy versus radial breathing mode frequency ( Energy vs 1/diameter) to form the Raman equivalent of the Kataura plot ( Energy vs diameter)[7]. Knowledge of the diameter and resonance energy $E_{ii}$ makes it possible to separate the RBM signatures of metallic from semiconducting tubes using the Kataura plot ($E_{ii}$ vs diameter), and for small diameter tubes where there are fewer chiralities / diameter, it may be possible to assign the chirality from resonant Raman spectra. Figure 3 shows an experimentally determined plot for individual nanotubes in solution for $E_{11}$ and $E_{22}$ semiconducting and $E_{11}$ metallic transitions. While it is possible to pair RBM frequencies with $E_{ii}$ obtained from full Raman excitation profiles to arrive at a nearly unambiguous chirality assignment for a specific RBM, the Kataura plot

may be used to help in assigning RBM features obtained in single excitation line spectra. The horizontal lines in Figure 3 show commonly used laser line energies: Ar-ion 488 nm (blue), 514.5 nm (green); HeNe 632.8 nm (red); and Ti-Sapphire 785 nm (magenta). The resonance window, which determines which specific chiralities will appear in a RBM spectrum excited at a given excitation wavelength, will depend strongly on the environment and varies from 10's of meV for a single nanotube to >140 meV for nanotubes in bundles. RBMs from nanotubes outside the resonance window of a selected excitation wavelength will not be observed. Furthermore, the resonance energies have been observed to shift depending on environment due to screening, with the highest resonance energies found for individual nanotubes in air, 10-30 meV lower for individual nanotubes in solution and ~ 100 meV lower for nanotubes in bundles.

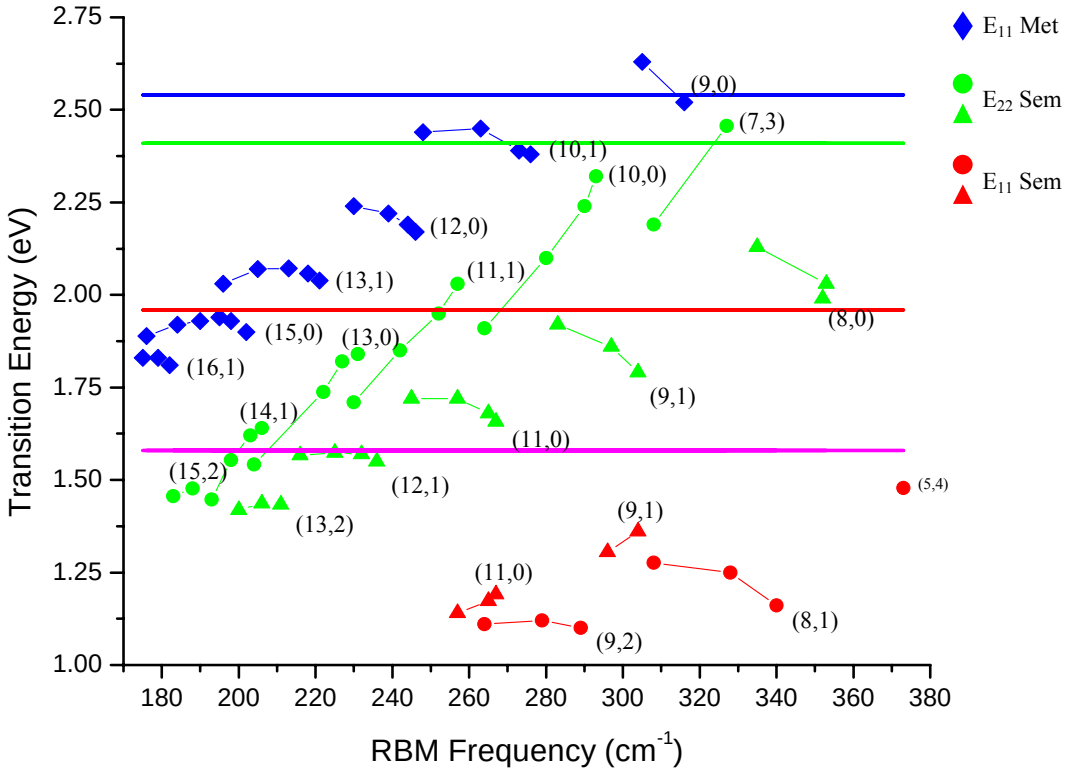


**Figure 3.** Experimentally determined Kataura plot for SWNTs in sodium dodecyl sulfate (SDS) solution. The colored horizontal bars represent different common laser energies (blue: 488 nm, green: 514.5 nm, red: 633 nm, magenta: 785 nm). Data points are grouped according to common 2n+m = constant families, with the near zigzag terminus of each family identified. For semiconducting tube types, circles represent chiralities with mod (n-m, 3) = -1, while triangles represent chiralities with mod (n-m, 3) = +1. Experimental data obtained from: S.K. Doorn, D.A. Heller, P.W. Barone, M.L. Usrey, M.S. Strano, *Appl. Phys. A*, **78**, 1147 (2004); C. Fantini, A. Jorio, M. Souza, M.S. Strano, M.S. Dresselhaus, M.A. Pimenta, *Phys. Rev. Lett.*, **93**, 147406 (2004); J. Maultzsch, H. Telg, S. Reich, C. Thomsen, *Phys. Rev. B*, **72**, 205438 (2005); and H. Telg, J. Maultzsch, S. Reich, C. Thomsen, *Phys. Rev. B*, **74**, 115415 (2006).

### 4.2.2 The G band

The G mode is a tangential shear mode of the carbon atoms. In graphite, there is one single G mode at ~1580 $cm^{-1}$. In carbon nanotubes, the single G band transforms into several modes due to the confinement of wave-vectors along the circumference. For chiral tubes, the G-band is composed of six modes with symmetries $A_{1g}$, $E_{1g}$ and $E_{2g}$ (two of each). The frequency of the higher energy branch, $G^+$ does not vary with diameter, while the low energy branch, $G^-$ gets softer for smaller diameter nanotubes. Examples of G-band structure from different carbon-based materials are shown in Figure 4 [8].

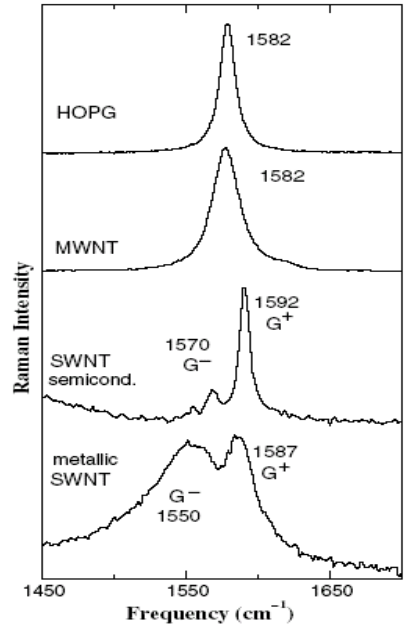


**Figure 4.** From [ 8]. G bands for graphite (HOPG), multiwall CNTs (MWNT), semiconducting and metallic SWNTs.

**Semiconducting nanotubes:** The highest mode, $G^+$=1590-1595 $cm^{-1}$ is a longitudinal optical (LO) shear mode parallel to the axis of the nanotube. Transverse optical (TO) shear modes perpendicular to the tube axis, $G^-$ modes, are softened due to the curvature or smaller diameters, and the frequency depends on the tube diameter. The G band line shapes are Lorentzian and relatively narrow even in a bundle for defect free nanotubes (FWHM~11 $cm^{-1}$).

**Metallic nanotubes:** The metallic tubes are easily recognized from the broad and asymmetric Breit-Wigner-Fano line-shape of the $G^-$ band. The frequency down shift of the $G^-$ is particularly strong for metallic nanotubes, with down shifts of the $G^-$ mode of ~100 $cm^{-1}$ for small diameter tubes. The $G^-$ energy decreases with decreasing diameter faster than for semiconducting nanotubes while the G+ remains essentially constant in frequency; see Figure 5 [9]. The line-shape was initially attributed to coupling between the $G^-$ phonons with low-lying optical plasmon corresponding to the tangential motion of the electrons on the nanotube surface. Recent work instead suggests that the coupling is due to a resonance between phonons and electron-hole pairs and that the assignment of the axial and circumferential assignments are reversed for metallic tubes, i.e., that the lower energy $G^-$ is a LO (axial) phonon mode [10].

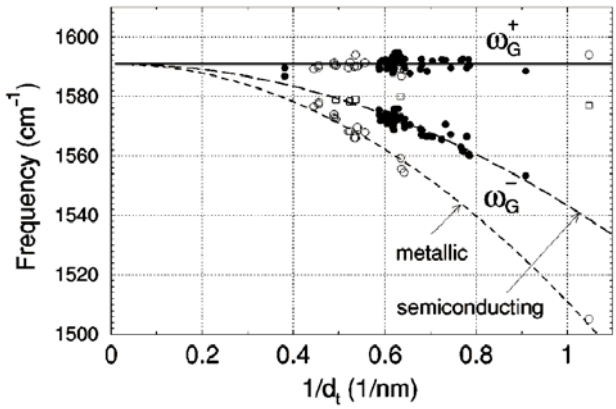


**Figure 5.** From [9] Measurements showing the diameter dependence of the $G^-$ band for metallic and semiconducting nanotubes

### 4.2.3 Second order Raman scattering, the D and G' modes (Zone boundary phonons)

The D and G' modes originate from longitudinal optical (LO) phonons from the vicinity of the K-point in the (graphene) Brillouin zone. The Raman D and G' are second order processes that involve e-phonon scattering from **k** + **q** via the zone boundary LO phonon, and scatters back to the **k** state either elastically via a defect (D band) or inelastically via a second LO phonon, and emits a photon by recombining with a hole at a **k** state.

**The D-band:** The D- band is called a defect mode because a defect is needed to elastically scatter from in order for the process to conserve momentum. The second order scattering described above can either be due to phonon-defect or defect-phonon scattering which yields two Raman peaks of slightly different energies. The quality of a sample is often evaluated by comparing the D to G band intensity, or the D to G' intensity. For high quality samples, without defects and amorphous carbon, the D/G ratio is often below a couple of percent. Examples of such low D/G ratios can be found in CVD-grown nanotubes[11] and in high quality laser oven-grown nanotubes[12].
Since different nanotubes have different resonance energies, the D band frequency is not fixed for different laser energies. Table 1 gives approximate values for four different laser lines. The D band is present in all carbon allotropes, including amorphous $sp^2$ and $sp^3$ carbon. The D band signal can originate from nanotubes with defects and/or from non-SWNT carbon. One way to identify the different contributions is by the line-shape of the D-band, where a broad peak (~100 $cm^{-1}$) is indicative of amorphous carbon. The d-band width for nanotube ensembles are ~10-20 $cm^{-1}$.

Figure 10 B in the Appendix shows the D and G band in double wall carbon nanotube powder before and after optical heating. The heating has removed much of the defect-rich carbon nanotubes and amorphous carbon as is evidenced from reduction of the D band intensity.

| Laser line (nm/eV) | 785 / 1.58 | 633 / 1.96 | 514 / 2.41 | 488 / 2.54 |
|---|---|---|---|---|
| D-band ($cm^{-1}$) | ~1290 | ~1330 | ~1345 | ~1360 |

**Table 1.** Approximate values for D band Raman shift with different laser excitation energies.

**The G' Band:** The G' band at frequencies 2500-2900 $cm^{-1}$ is the second order process from two zone boundary LO phonons with wave vectors *q* and -*q*, thus automatically preserving the momentum conservation constraint. Therefore, the G' band is an intrinsic property of the nanotube and graphite, and present even in defect-free nanotubes where the D band is completely absent. The frequency of the G' band is close to twice the D-band frequency. The dispersion of the G' band is $\omega_{G'}$ ~ 2420 $cm^{-1}$+105 $cm^{-1}$/ $E_{laser}$ (eV).

**Incoming and outgoing (scattered) resonances:** The energy of a G' band is substantial, (~0.33 eV). In ensemble measurements, nanotubes can be resonant either with the incoming laser energy, or with the (lower) scattered energy, and both scattering events will contribute to the signal. Incoming and outgoing scattering resonances will result in G' bands at different energies due to the energy dispersion of the G' band. Sometimes, the incoming and scattered light matches a nanotube electronic structure so well that the incoming and scattered light can both be resonant with two different $E_{ii}$'s from one particular nanotube. In this case, two G' peaks at different energies are observed from the same nanotube, due to the energy dispersion of the phonon modes near the zone boundary as is illustrated in Figure 6.

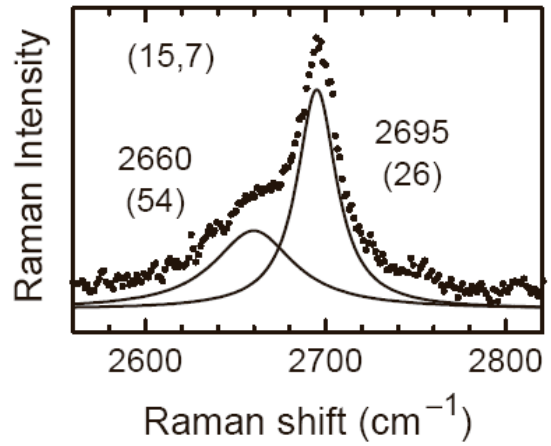


**Figure 6**. a) 2 G' peaks from a (15,7) nanotube where the incident $E_L$ = 2.41 eV and the scattered $E_L - E_G$ =2.08 eV light. The resonant energies are $E_{33}$ =2.19 eV and $E_{44}$ =2.51 eV. From [13]

## 4.3 Width of the Resonance

It is of interest to know the width of the resonance to determine how far away from a resonance it is possible to get a Raman RBM signal. The incoming resonance is peaked around $E_{ii}$ and the outgoing resonance is a phonon energy higher (Stokes) or lower (anti-Stokes). The width of the resonance window is approximately the sum of the RBM energy + the resonance broadening $\gamma$.

*Ensemble measurements* [7]

- *Solution:* The broadening $\gamma$ has been measured to be $\gamma$ ~ 60 meV for nanotubes dispersed in sodium dodecyl sulfate solution.
- *Bundles*: For nanotubes in thick bundles the broadening is $\gamma$ ~120 meV.

*Individual measurements* [5]

- For (nearly) individual nanotube measurements suspended in air or on substrates, the width $\gamma$ varies from $\gamma$ =10 – 40 meV.

## 4.4 Strength of the Raman Signal; electron–phonon coupling

Apart from the electronic resonance condition that controls the strength of the Raman signal, the peak intensity also depends on the electron-phonon (e-ph)

coupling. This is an active area of research with constant updates in the literature. Both measurements and calculations agree that there is a strong chirality and diameter dependence of the e-ph coupling for the radial breathing modes as well as a dependence on which $E_{ii}$ is active. For semiconducting nanotubes, the Raman scattering cross-section is proportional to

$$|M_{e-ph}|^2 = \left| \frac{a(E_{ii})}{d_t^2} + \nu \frac{b(E_{ii})}{d_t} \cos 3\theta \right|^2$$

where the constants *a* and *b* depend on which electronic energy level $E_{ii}$ is excited, $\nu$ is the chiral index -1 or 1 [14] . Hence, when determining chirality distributions from Raman RBM intensities one has to take into account the chirality dependent e-ph coupling strength [15 ].

## 4.5 Depolarization and Selection rules

The largest Raman intensity will be generally observed for light polarized along the tube axes, and almost no signal will be observed for cross-polarized light. The intensity varies as $\cos^4\theta$, where $\theta$ is the relative angle between the electric field, E, and the nanotube axis. The angular dependence can be used to measure the degree of alignment, e.g. carbon nanotubes dispersed in a polymer matrix.

The decrease in signal for polarization perpendicular to the nanotube axis is due to depolarization or the antenna effect. Light with an external electric field vector parallel to the nanotube axis, $E_{||}$, does not induce a polarization, and the total field is equal to the external field. On the other hand, an electric field perpendicular to the nanotube axis, $E_{\perp}$, induces charges on the two opposing sides of the wall. The effect is a large opposing depolarization field that reduces the external field $E_{\perp}$. The antenna effect is a strong effect for narrow nanotubes <2 nm.

The resonance with the $E_{ii}$ transition for light polarized parallel to the nanotube axis is due to angular momentum conservation which requires $\Delta m$=0 for $E_{||}$ where *m* is the angular momentum quantum number. For a perpendicular field $E_{\perp}$ the angular momentum conservation requires $\Delta m=\pm 1$, i.e., $E_{ij}$ with j= $i\pm 1$. Due to the depolarization effect, $E_{ii}$ transitions are favored over $E_{ij}$ transitions.

## 4.5 Practical Considerations

### 4.5.1 Measurement setup

A variety of commercial Raman instrumentation is available for characterization of nanotube samples. Instrumentation ranges from relatively inexpensive (~$10K) fixed wavelength benchtop systems with common excitation wavelengths of 532 nm, 633 nm, or 785 nm. Higher sensitivity single wavelength systems based on high-throughput spectrographs incorporating holographic

diffraction gratings and notch filters are also available at higher cost. For studies of single nanotubes in very disperse samples, micro-Raman instrumentation is used which consists of a microscope coupled to a spectrometer with a CCD camera, and one or more laser excitation sources.
More versatile scanning Raman systems may be assembled from commercially available triple spectrographs coupled to tunable excitation sources such as Ti:sapphire and dye lasers. Similar excitation tunability may be coupled to micro-Raman systems.

In all systems, the spectrometer grating should be chosen to have a large throughput for the laser line(s) used, and to give the desired spectral resolution, preferably 3 $cm^{-1}$ or better.

## Calibration and Alignment

If several laser lines are used it is necessary to re-align optical paths and calibrate the frequencies after each line switch, and the practitioner should follow standard alignment procedure.

Before each set of measurements a quick check of alignment and calibration should be done:
Calibration of grating reading:

- Check that the Stokes and anti-Stokes peak frequencies are symmetric around the laser line for the test sample.
- A general calibration is needed with well-known lamp lines, such as those from helium, neon or krypton for absolute frequency measurements and to assign the spectral resolution. These can be compared with known values found at http://physics.nist.gov/PhysRefData/ASD/lines_form.html . Other Raman shift standards such as acetamidophenol (Tylenol) or cyclohexane may also be effectively used for spectral calibration. See the McCreery group website: http://www.chemistry.ohio-state.edu/~rmccreer/freqcorr/shift.html
- For tunable laser sources, an optical wavemeter can be used to calibrate the laser energy.

Optical path alignment for micro-Raman instruments:

- Adjust the excitation path so that the laser light goes straight through the objective: when adjusting the z-position in and out of focus, the laser spot should expand symmetrically. If not, the spectral calibration will be off and collection efficiency lowered.
- Use a calibration sample with a strong and well known Raman line, e.g., the ~521 $cm^{-1}$ Raman line from polished silicon (100). Align the Si (110) direction with the laser polarization. Check that the Si Raman signal is maximized for a given wavelength, laser power and slit width. Record the signal /second for a specific power for comparison.

## 4.5.2 Laser power heating effects

It is relatively easy to unintentionally heat the sample by optical heating, especially when using a Raman microscope, in which the laser light is focused to a small focal volume with a resulting high power density. Optical heating of the sample could possibly damage the sample by burning, and also change the resonance energies which decrease with temperature. Therefore, sufficient sample heating will result in resonance with a different subset of the sample, and yield different spectra at different temperatures. It is only when a (nearly) single nanotube is studied that one can determine the actual effect of heating on the Raman spectra. For bulk measurements, any change is convoluted by resonances with a different subset of nanotubes in the sample. The laser powers that can be safely used without significant heating depend both on laser energy and on sample preparation as discussed below. More details are given on this topic in the Appendix.

### Diagnostics

The $G^+$ mode frequency can be used as a thermometer. In the literature, frequency shifts of the $G^+$ mode with temperature from -0.022 to -0.048 $cm^{-1}/K$ have been reported. To avoid excessive heating, the power should be lowered until the $G^+$ stays constant in energy.

The Stokes/anti-Stokes intensity ratio for the radial breathing modes is also an indictor of the temperature, and a change in this ratio with laser power is also an indication of excess laser heating. However, this ratio is more complex to interpret since the ratio depends both on temperature and the resonance energy. For example, if $E_{laser} \geq E_{ii}$ at $T_1$ and the temperature increased to $T_2$, the change in resonance condition will tend to decrease the $I_{AS}/I_S$ ratio while the Boltzmann factor favors an increase in the $I_{AS}/I_S$ ratio with increasing temperature.

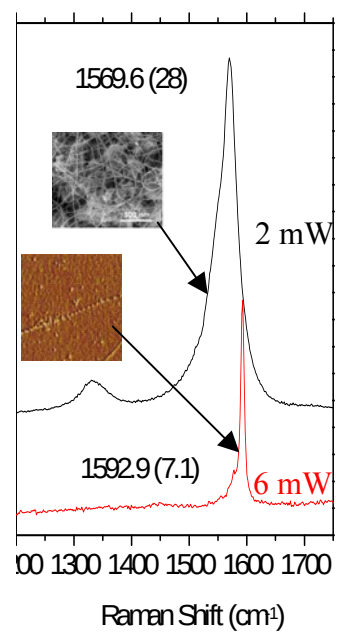


**Figure 7.** G band from powder and from individual nanotube on substrate. Heating effects are clearly seen for the powder where the G band is down shifted 23 $cm^{-1}$ while the single tube is unaffected at 3 times the power.

### Sample type

The physical state of the sample (and the degree of impurities) plays a large role in choosing a suitable laser power. Samples with a higher degree of graphitic impurities heat more easily, presumably since the effective thermal conductivity of the graphitic impurities are not as high as for nanotubes, see Figure 7.

Individual nanotubes dispersed in solution with a surfactant will heat significantly less than a dry powder/ bundles in air, and individual nanotubes on a substrate are also efficient in dissipating heat. The heating of nanotubes in a polymer

matrix will depend on the degree of dispersion of the nanotubes and heat conductivity and heat capacity of the polymer.

We recommend using $< 3\ 10^5$ W/cm$^2$ for samples in solution and for individual nanotubes on a substrate, and $<10^4$ W/cm$^2$ for powders and dispersions in polymers and to check whether a decrease in power will further shift the $G^+$ band frequency.

### 4.5.3 Material inhomogeneity

Carbon nanotube powder varies in composition on a micrometer scale. Therefore it is recommended that several spectra are collected from different sample positions to get a statistically meaningful measurement. A second approach is to collect signal from a larger area.

**Sample preparation**
Since environment and the degree of nanotube aggregation will influence e.g. excitation window, excitation energy and degree of heating, it is necessary to prepare samples that will be compared in the same way. Whether raw, dry material, or formed into a pellet, or dissolved into solution, or dispersed on filter paper, or isolated, each sample preparation brings its own unique features to the Raman spectra and therefore should be considered during analysis.

**Solution preparation:** Typical preparation of solution samples of nanotubes begins with high shear mixing of the nanotubes in a 1% aqueous solution of surfactant. The suspension is then ultrasonicated at high power with tip or cuphorn sonicators (typically for 10 minutes). Samples are then ultracentrifuged. Four hour centrifuge times work well, with acceleration force chosen depending on nanotube production method. For HiPco nanotubes, an acceleration force of 110,000 g works well, while lower forces (60-70,0000 g) works better for samples with small diameter distributions (such as those produced in the CoMoCat process). Centrifuged samples will show separation between pelleted aggregates (found at the bottom of the centrifuge tube) and individualized nanotubes, which are decanted off. Common surfactants are sodium dodecyl sulfate (SDS), sodium dodecylbenzene sulfate (SDBS), sodium cholate, and even direct suspension into single or double stranded DNA. SDBS is known to give the most blue-shifted excitation spectra of any of the listed surfactants. For large diameter nanotubes, such as those produced in laser-oven methods, sodium cholate or polymeric surfactants (such as Triton-X 100 or Pluronic) may be most suitable for sample suspension. Solution spectra are readily obtained from samples contained in NMR or melting point capillary tubes.

# 4.6 Appendix

## *4.6.1 Illustration of Aggregation Effects*

As noted above, sample state and environment will have a significant effect on features observed in SWNT Raman spectra, particularly in the RBM region. These effects are primarily due to shifting and broadening of the electronic transitions. These effects are most pronounced in comparing solution to aggregated samples. Figure 8 illustrates the significant red-shifting and broadening of excitation profiles for the (12,1) and (10,2) chiralities that occurs upon nanotube bundling. As seen in Figure 9, such changes in excitation spectra can lead to very different features appearing in RBM spectra at a given excitation wavelength.

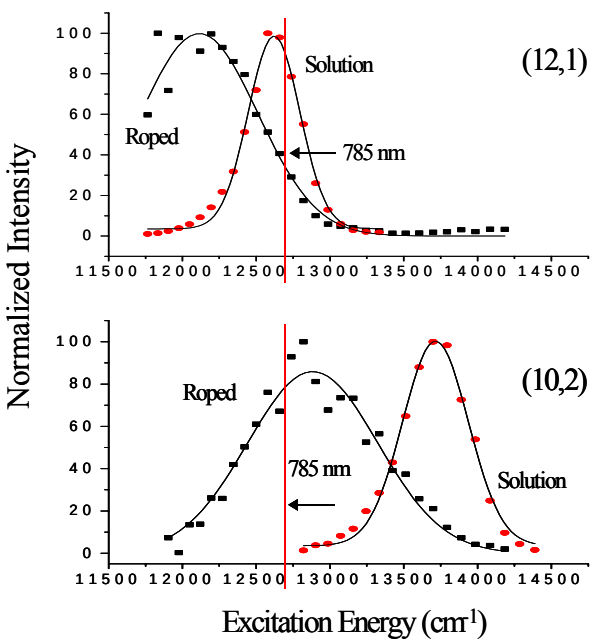


**Figure 8.** Comparison of Raman excitation profiles of SDS solubilized and bundled nanotubes for the (12,1) and (10,2) chiralities. The vertical line represents the 785 nm excitation line position.

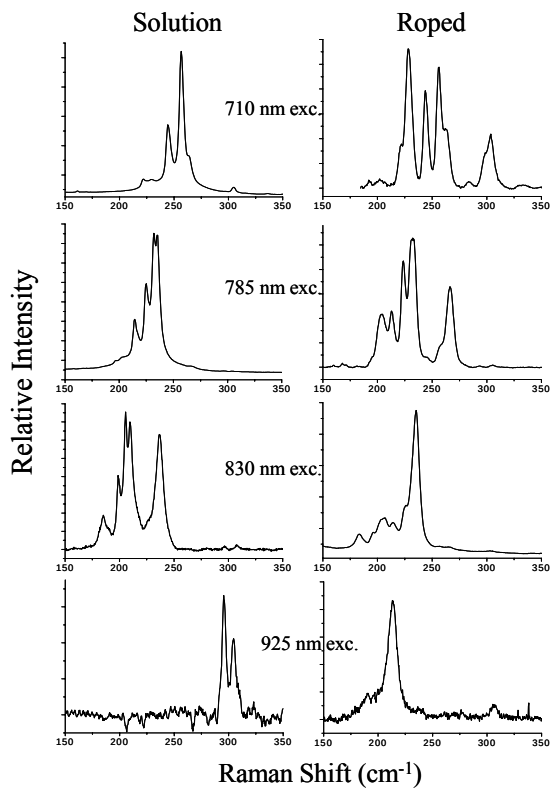


**Figure 9.** Comparison of RBM spectra for SDS solubilized and bundled nanotubes at four specific excitation wavelengths.

Such effects underscore the importance of understanding the effects of electronic perturbation on observed RBMs. This is particularly relevant to the use of Raman for characterization of separations processes. Care must be taken to ensure that observed changes in relative RBM intensities are not incorrectly attributed to changes in relative populations of their corresponding chiralities, when the cause may instead be a shift in electronic transition energies that brings a different set of chiralities into resonance with a specific excitation wavelength.

As illustrated in Figs. 8 and 9, the use of 785 nm excitation can be a practical means for probing the extent of nanotube aggregation. Bundling of nanotubes results in increased enhancement of the (10,2) RBM at 265 $cm^{-1}$, relative to nearby RBMs (including the (12,1) mode at 236 $cm^{-1}$), producing the so-called roping peak. Note that, while the (10,2) RBM at 265 $cm^{-1}$ is strongly observed only in the bundled sample with 785 nm excitation, the (12,1) RBM at 236 $cm^{-1}$ appears strongly enhanced in both sample types. This behavior results from the different resonant excitation conditions experienced by the two chiralities. As seen in Figure 8, 785 nm excitation is near the peak of the excitation profile for the individualized (12,1) nanotubes, but is well away from the resonance window for the (10,2) in solution. Thus, the (12,1) RBM is observed but not the (10,2). Bundling-induced red-shifting places the 785 nm excitation near the peak of the (10,2) transition, while significant intensity in the tail of the (12,1) profile still remains. Therefore, for bundled samples, both the (12,1) and (10,2) chiralities will be observed.

### 4.6.2 Illustration of heating effects

Figure 10 shows the effects of optically heating a sample of double wall carbon nanotube powder. As the optical power is increased, the G band is dramatically shifted down in frequency due to heating. Here 100% power corresponds to 8

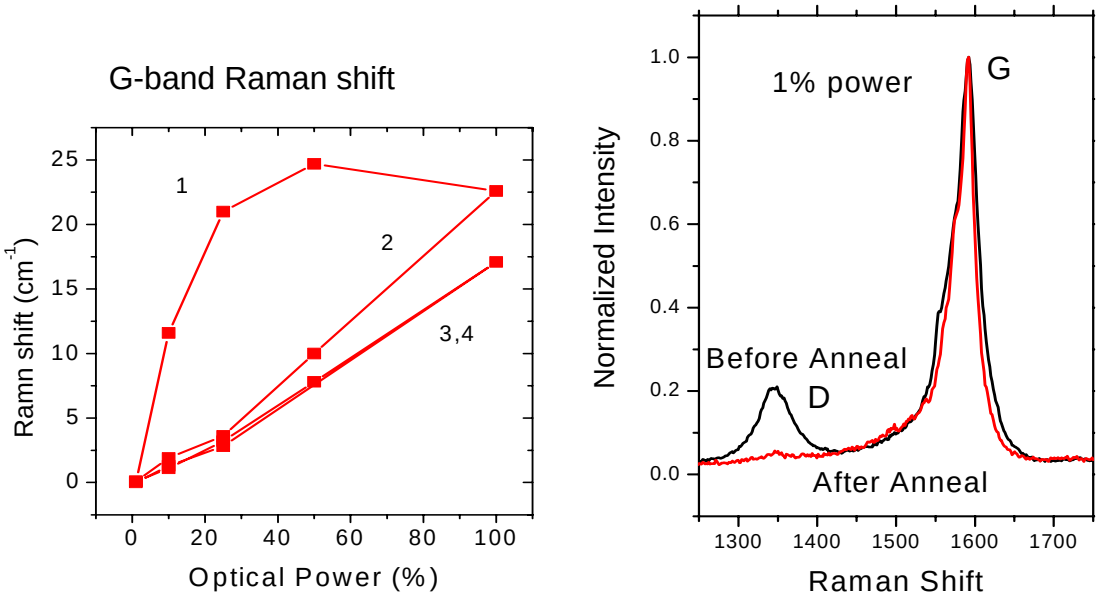


**Fig.10** Effect of optical heating of a powder sample. G band Raman shift indicative of optical heating of DWNT powder using 514 nm laser. 100% power =8 mW with *NA*=0.8 objective. A) Down-shift in the G+ mode as a function of optical power. The numbers indicate the time sequence of the measurements B) Raman spectra at low power (no heating) before and after thermal cycling shows the reduction of the D band intensity and line-width after heating.

mW optical power at 514 nm with a *NA*=0.8 objective ( ~$10^6$ W/cm$^2$). The maximum shift of the G band corresponds to a sample temperature increase of ~480 C using the most conservative estimate of 0.048 cm$^{-1}$/K. Subsequent cycles of increasing and decreasing the optical powers show a less marked heating than the first increase, Fig 10a. This behavior can be correlated to the removal of carbon impurities and nanotubes with defects shown in Fig. 10 b), which shows the reduction in the D band intensity after the local optical heating.

The D band disappears as the temperature is increased, and during subsequent power cycling the temperature increases less. These results illustrate that a sample with large D band tends to heat more readily than a more ideal nanotube sample, and that heating can remove the defects, either by annealing defects or the physical "burn off" of the defective material.

### 4.6.3 Measurements from one individual nanotube - "nano-slit effect"

In confocal microscopy, a pinhole is used in the image plane of the microscope system to limit the area and the depth from which the signal is collected from the sample. Confocal techniques are used for mapping an image at different depths (confocal sectioning), e.g. mapping nanotube composite depth profiles, although the penetration depth will limit the depth information that is possible to extract. When confocal microscopy is used from a sparse sample, the nano-scaled object will act as 'nano-slit", and a slight displacement of the nano-particle from the optical axis will lead to false shifts in the measured Raman frequency.

Knowing the resolution of the spectrometer, detector pixel size, and the overall magnification from object plane to detector, this "pseudo-shift" is easily calculated for a given distance in the spectral direction of the emitter from the optical axis. The "nano-slit" effect is illustrated in Fig 11 a) by measuring the shift RBM frequency as a function of position stepping across the nanotube oriented parallel

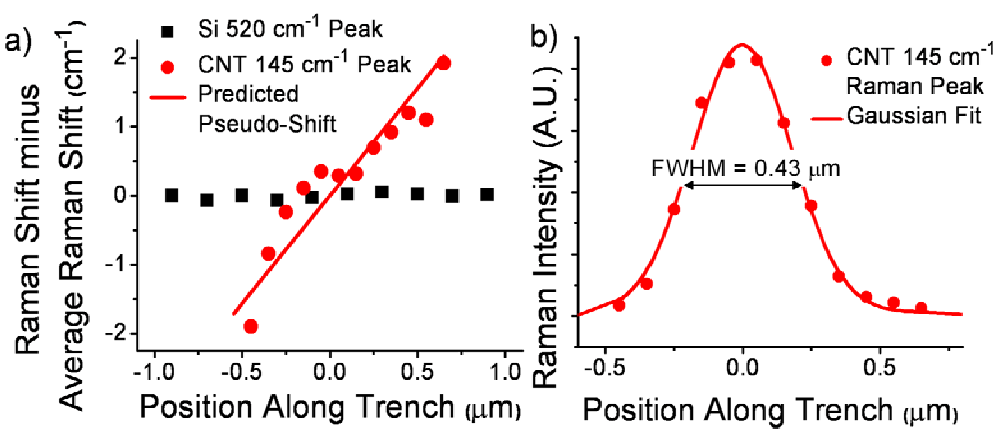


**Figure 11** a) from [5] False Raman shift as a function of horizontal displacement of a single nanotube (in red). b) Measurement of the optical beam profile at the focal plane using a nanotube.

to the groove direction of the spectrometer grating. For comparison, the silicon 521 $cm^{-1}$ Raman peak from the substrate is also shown. The silicon signal originates from all points illuminated by the beam spot and is unaffected by translation and consequently does not shift with sample position.

The “nanoslit” configuration also provides an elegant method for directly measuring the profile of the beam intensity in the object plane. An example is shown in Fig.11b).

## Acknowledgements

We would like to thank Angela Hight Walker of NIST, Gaithersburg, Apparao Rao of Clemson University and Victor Hadjiev of University of Houston for critical reading of the manuscript. Special thanks to Sivaram Arepalli at NASA-Johnson Space Center and Steve Freiman of NIST for coordinating the effort, and for their continuous support and advice.

## References

1 **Introductory Raman Spectroscopy** by John Ferraro, *Academic Press*, (2002); **Modern Raman Spectroscopy** by Ewen Smith and Geoffrey Dent, *Wiley*, (2005).

2. **Physical Properties of Carbon Nanotubes** by R Saito, G. Dresselhaus and MS. Dresselhaus *Imperial College Press* (1998) **Carbon Nanotubes: Basic Concepts and Physical Properties** by Stephanie Reich, Christian Thomsen, and Janina Maultzsch, *Wiley* 2004; H. Kataura, Y. Kumazawa, Y. Maniwa, I. Umezu, S. Suzuki, Y. Ohtsuka and Y. Achiba, *Synthetic Metals* **103** pp. 2555-2558 (1999); M. S. Dresselhaus, G. Dresselhaus, A. Jorio, *Annu. Rev. Mater. Res*. **34**, 247 (2004)

3 J. Maultzsch, R. Pomraenke, S. Reich, E. Chang, D. Prezzi, A. Ruini, E. Molinari, M. S. Strano, C. Thomsen, and C. Lienau, *Phys. Rev. B* **72**, 241402(R) (2005); Wang F, Dukovic G, Brus LE, Heinz TF *SCIENCE* **308** (5723): 838-841 (2005)

4 A. N. Vamivakas, A. Walsh, Y. Yin, M. S. Ünlü, B. B. Goldberg, and A.K. Swan, accepted, *Phys Rev B* **74** (2006)

5. Y. Yin, A. G. Walsh, A. N. Vamivakas, S. Cronin, A. M. Stolyarov, M. Tinkham, W. Bacsa, M. S. Ünlü, B. B. Goldberg, and A. K. Swan, Accepted, *J. Special topics in quantum electronics* (2006)

6. M.S. Dresselhaus, G. Dresselhaus, R. Saito, A. Jorio *Physics Reports* **409** 47–99 (2005)

7. S.K. Doorn, D.A. Heller, P.W. Barone, M.L. Usrey, M.S. Strano, *Appl. Phys. A*, **78**, 1147 (2004); C. Fantini, A. Jorio, M. Souza, M.S. Strano, M.S. Dresselhaus, M.A. Pimenta, *Phys. Rev. Lett*., **93**, 147406 (2004); J. Maultzsch, H. Telg, S. Reich, C. Thomsen, *Phys. Rev. B*, **72**, 205438 (2005); and H. Telg, J. Maultzsch, S. Reich, C. Thomsen, *Phys. Rev. B*, **74**, 115415 (2006).

8. A Jorio, M A Pimenta, A G Souza Filho, R Saito, G Dresselhaus and M S Dresselhaus, *New Journal of Physics* **5** 139.1 (2003)

9. Jorio de Vasconcelos, A. G. Souza Filho, G. F. Dresselhaus, M. S. Dresselhaus, A. K. Swan, M. S. Ünlü, B. B. Goldberg, M. A. Pimenta, J. H. Hafner, C. M. Lieber, and R. Saito, *Phys. Rev. B*, **65,** 155412 (2002)

10 Lazzeri M, Piscanec S, Mauri F, A. C. Ferrari, and J. Robertson PHYS. REV. B **73**155426 (2006)

11. S.K. Doorn, L. Zheng, M.J. O’Connell, Y. Zhu, S. Huang, J. Liu, *J. Phys. Chem*., **109**, 3751 (2005)

12. A.C. Dillon, P.A. Parilla, J.L. Alleman, T. Gennett, K.M. Jones, M.J. Heben, *Chem. Phys. Lett*., **401**, 522 (2005)

13. A.G. Souza Filho, A. Jorio, Anna K. Swan, M.S. Ünlü, B.B. Goldberg, R. Saito, J.H. Hafner, C.M. Lieber, M.A. Pimenta, G. Dresselhaus, M.S. Dresselhaus, Anomalous two-peak *G*_-band Raman effect in one isolated single-wall carbon nanotubes, *Phys. Rev. B* **65** 085417 (2002)
14 SV Goupalov, BC Satishkumar, SK Doorn, *Phys.Rev. B* **73** 115401, (2006)
15. Maultzsch J, Telg H, Reich S, Thomsen, *Phys.Rev. B* **72**, 205438 (2005); Y. Yin, A. Vamivakas, A. Walsh, S. Cronin, M. S. Unlu, B. B Goldberg, A. K. Swan *cond-mat*/0605670; A. Jorio, A.P. Santos, H.B. Ribeiro, C. Fantini, M. Souza, J.P.M. Vieira, C.A. Furtado, J. Jiang, R. Saito, L. Balzano, D.E. Resasco, M.A. Pimenta, *Phys. Rev. B*, **72**, 075207 (2005); and Z. Luo, F. Papadimitrakopoulos, S.K. Doorn, *Appl. Phys. Lett.*, **88**, 073110 (2006).